

# Topological properties of curved spacetime Su–Schrieffer–Heeger model

Priyanuj Rajbongshi<sup>1,\*</sup> and Ranjan Modak<sup>1,†</sup>

<sup>1</sup>*Department of Physics, Indian Institute of Technology Tirupati, Tirupati 517619, India*

The Su–Schrieffer–Heeger (SSH) model, a prime example of a one-dimensional topologically nontrivial insulator, has been extensively studied in flat space-time. In recent times, many studies have been conducted to understand the properties of the low-dimensional quantum matter in curved spacetime, which can mimic the gravitational event horizon and black hole physics. However, the impact of curved spacetime on the topological properties of such systems remains unexplored. Here, we investigate the curved spacetime (CST) version of the SSH model by introducing a position-dependent hopping parameter. We show, using different topological markers, that the CST-SSH model can undergo a topological phase transition. We find that the topologically non-trivial phase can host zero-energy edge modes, but those edge modes are asymmetric, unlike the usual SSH model. Moreover, we find that at the topological transition point, a critical slowdown takes place for zero-energy wave packets near the boundary, indicating the presence of a horizon, and interestingly, if one moves even a slight distance away from the transition point, wave packets start bouncing back and reverse direction before reaching the horizon. An extended version of the CST-SSH model, which supports distinct topological phases characterized by higher winding numbers, has also been studied. We show that a similar critical slowdown of wave packets near the boundary occurs at all topological transition points between any two distinct phases. A semiclassical description of the wave packet trajectories also supports these results.

## I. INTRODUCTION

One of the most astonishing predictions of Einstein’s theory of general relativity [1] is the potential existence of black holes, i.e., space-time regions from where nothing can escape. From then on, there have been efforts to simulate a black hole horizon and the relevant curve spacetime (CST) physics in the laboratories. In 1981, Unruh proposed a sonic horizon, which is based on the observation that sound waves in flowing fluids, in appropriate conditions, can be described by the same wave equation as a scalar field in a curved space-time. The acoustic horizon occurs if the velocity of the fluid exceeds the speed of sound within the liquid, acting on sound waves exactly as a black hole horizon does [2, 3]. Further, there exist proposals for black hole analogs, analogue Hawking radiation, and other curved spacetime phenomena analogs based on light propagation in dielectric media, liquid Helium 3, and Bose-Einstein condensates, classical electronics circuits, Floquet quantum systems [4–18]. These works have provided a setup for studying the CST physics in laboratories, which has deepened the understanding of the curved spacetime and gravity, e.g., one of the milestones of these studies was to reveal the relation between (1 + 1)D Jackiw-Teitelboim gravity and the Sachdev-Ye-Kitaev model [19–21]. Only in the last few years, there have been some studies that have focused on the condensed matter properties in CST lattice systems, asking extremely fundamental questions like what will happen to the fate of thermalization and localization in CST lattice models [22–25].

On the other hand, one of the main goals of condensed matter physics is to deal with different phases of matter. Traditionally, phase transitions were characterized by order parameters within Landau’s free-energy theory framework and

symmetry breaking. In the past few decades, the identification of new phases of matter that did not break any symmetry, nor could be characterized by the usual order parameters, has led to the appearance of topology in condensed matter systems. While 2D electronic systems, which displayed a quantized Hall conductance [26], are probably 1st known example of such a condensed matter system where topology plays a crucial role, in recent days, a new class of electronic materials such as topological insulators [27–32], topological crystalline insulators [33–35], and topological semimetals [36–39] have emerged as a material having nontrivial Bulk band topology that can be exploited for application in low-power consumption electronic and spintronic devices due to the robustness of their edge states to defects, which are topologically protected. In this context, to understand how these materials behave in realistic situations, it is important to first understand simple toy models that show such a topological phase transition. One such example of a toy model is the one-dimensional (1D) Su–Schrieffer–Heeger (SSH) model, which is an example of a topological insulator [40]. It is a tight-binding model of non-interacting spinless electrons confined in a dimer chain, and has been extensively studied both theoretically and experimentally in the recent past [41–45]. The SSH model was initially introduced to describe a 1D chain of polyacetylene, on which electrons hop with staggered hopping amplitudes. There are two sites in each unit cell of this model; thus, it is a two-band model, and has winding number as its corresponding topological invariant. In particular, the number of edge states on a boundary of the system has a one-to-one correspondence to the winding number associated with this model.

In this work, our main goal is to connect these two extremely different branches of physics, 1) curved spacetime and black hole, and 2) topological systems in condensed matter. We propose a CST lattice model inspired by the two-band SSH model. First, we investigate whether we can see the event horizon physics or not. Next, we investigate whether the CST version of the SSH model has a topologically non-trivial phase or not. Remarkably, we answer both questions affirmatively in

\* ph24d004@iittp.ac.in

† ranjan@iittp.ac.in

this manuscript. We show using different topological markers that the CST-SSH model also shows a topological phase transition. Most interestingly, exactly at the transition point, a critical slowdown takes place for zero-energy wave packets, which indicates the presence of a horizon. The same phenomenon has also been observed in the extended version of the CST-SSH model at all topological transition points.

This paper is organized as follows: We define our CST-SSH model in Section II. Section III shows the wave packet dynamics and semi-classical analysis of the dynamics. We investigate the gap of the spectrum and also the zero-energy states in Sec. IV. We dedicate the Sec. V for different topological markers to check the topological nature of the model, and Sec. VI shows the effect of quench across different topological phases in CST-SSH. Section VII is dedicated for the extended version of the CST-SSH model. Finally, we summarize our findings in Sec. VIII.

## II. CURVED SPACETIME SSH MODELS

In some recent studies [25, 46], an equivalence between the Dirac equation in curved spacetime and a tight-binding condensed matter system with power law position-dependent hopping has been demonstrated. As suggested, we can establish a direct connection between the continuum field theory and a condensed matter system by considering a simple tight-binding Hamiltonian in real space with nearest-neighbor (nn) position-dependent hopping:

$$\mathcal{H} = - \sum_{n=1}^{N-1} t_n (c_n^\dagger c_{n+1} + h.c.), \quad (1)$$

where  $c_n^\dagger$  and  $c_n$  are fermionic-creation and annihilation operators, and  $t_n$  is a position-dependent hopping parameter. In the thermodynamic limit, if  $t_n = t$  (the nn hopping amplitude is constant for all sites), then the Hamiltonian can be diagonalized very easily in the momentum space  $k$ . The Hamiltonian will read as,  $\mathcal{H} = \sum_k \varepsilon(k) c_k^\dagger c_k$ , where  $c_k^\dagger$  and  $c_k$  are creation and annihilation operators in momentum space, and  $\varepsilon(k) = -2t \cos k$ . In case of position-dependent hopping  $t_n$ , with  $N \rightarrow \infty$ , we can approximate the local band structure for the bulk as  $\varepsilon(n, k) \sim -2t_n \cos k$ , and the local Fermi velocity as  $v_F(n) \sim \pm 2t_n$ . Thus, the local velocity varies with spatial coordinates, as the hopping here is position-dependent. In the continuum limit, these kinds of lattice models are equivalent to a massless Dirac field with the two-component spinor  $\hat{\Psi} = (\hat{\Psi}_+, \hat{\Psi}_-)^T$  that obeys the following time-evolution equation [46],

$$\partial_\tau \hat{\Psi} = \sigma_3 \left( v(x) \partial_x + \frac{1}{2} \frac{dv}{dx} \right) \hat{\Psi}, \quad (2)$$

where,  $\sigma_i$ , ( $i = 1, 2, 3$ ) are the Pauli matrices and  $v(x)$  is a position-dependent velocity, relating to the hopping as  $v(x) = 2t(x)$ . It is identical to the Dirac equation on (1+1) D spacetime in the massless limit. Thus, Eq. 1 is the low-energy discrete version of a Dirac Hamiltonian in the continuum limit

with the equation of motion 2, and with the Rindler metric

$$ds^2 = -v^2(x) d\tau^2 + dx^2. \quad (3)$$

At  $v(x) = 0$ , i.e.,  $t(x) = 0$ , this Rindler metric possesses an event horizon, as at that point, the local speed of light goes to zero. If we let  $t(x) \propto x^\sigma$ , where  $\sigma$  is indicating the warping of spacetime [22], at  $x = 0$ , the lattice model will possess event horizon for  $\sigma \geq 1$ : an gaussian wave-packet propagating in this lattice will suffer eternal slowdown and never reaches the origin, thus effectively forming an event horizon at the origin in the lattice model.

In a similar spirit, in this work, we study the curved-spacetime version of the SSH model, which is described by the following Hamiltonian,

$$H = \sum_{n=1}^N t_1(n) c_{n,A}^\dagger c_{n,B} + \sum_{n=1}^{N-1} t_2(n) c_{n,B}^\dagger c_{n+1,A} + h.c. \quad (4)$$

where  $c_{n,A}^\dagger$ ,  $c_{n,A}$  ( $c_{n,B}^\dagger$ ,  $c_{n,B}$ ) are fermionic creation and annihilation operators at the A sub-lattice (B sub-lattice) of the  $n$ th unit cell and  $t_1(n) = t_1 \left( \frac{2n-1}{2N-1} \right)^\sigma$  and  $t_2(n) = t_2 \left( \frac{2n}{2N-1} \right)^\sigma$ .

In the  $\sigma = 0$  limit, the model maps exactly to the usual SSH model, which has a topologically non-trivial (trivial) phase when  $t_1 < t_2$  ( $t_1 > t_2$ ), and is followed by a topological transition when  $t_1 = t_2$  [40]. We identify  $t_1$  and  $t_2$  as the intra- and inter-cell hopping strengths, respectively.

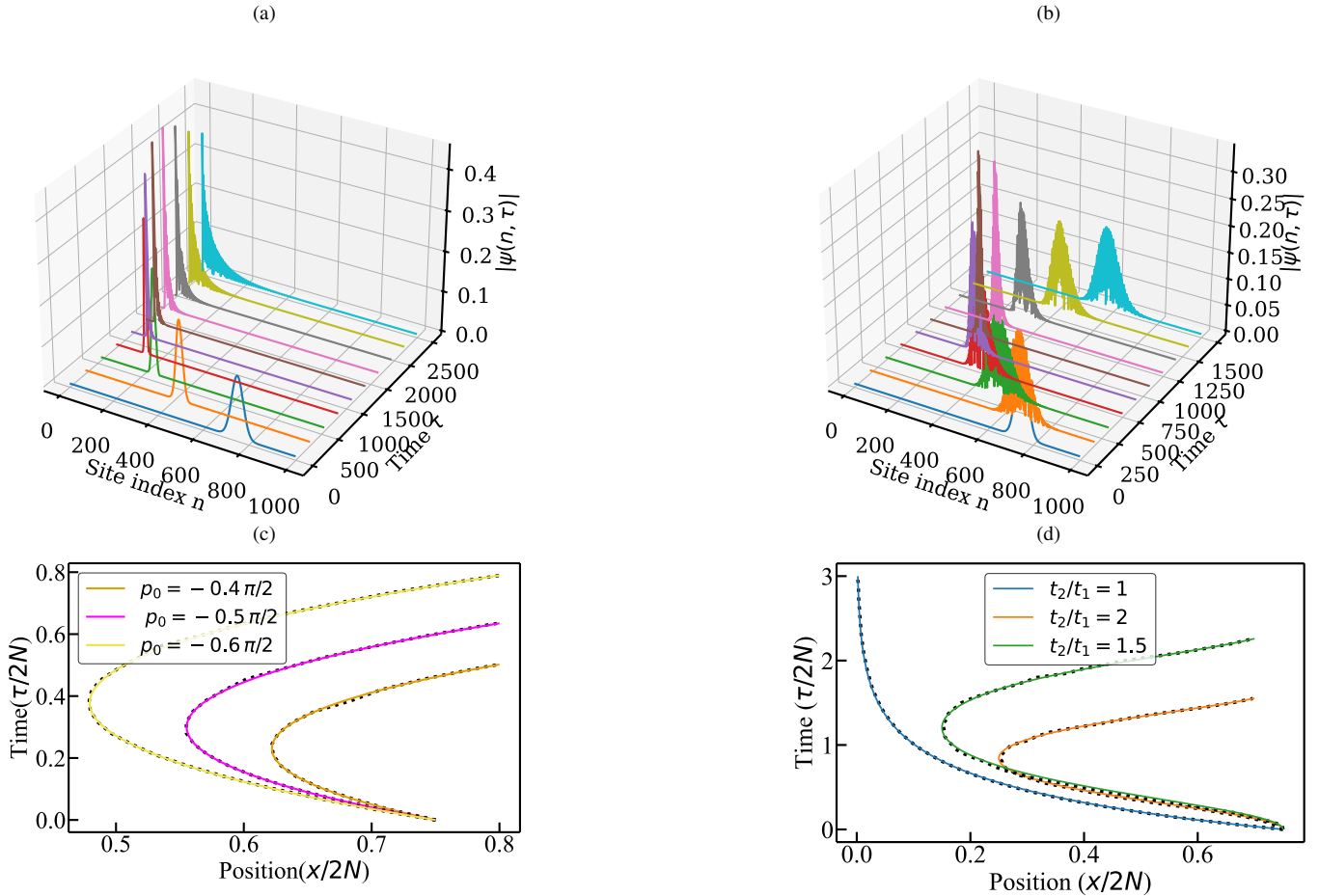
We also consider an extended version of the SSH model, where the hopping is not just restricted to between nearest neighbors, but higher-order hopping has also been allowed. In the context of the standard SSH model, a similar model was studied in Ref. [47, 48], which is known as the extended SSH model. Here we study the CST version of such models, where hopping is position-dependent, and the model reads as,

$$H_{ext} = \sum_{n=1}^N \left( t_1(n) c_{n,A}^\dagger c_{n,B} + t_2(n) c_{n,B}^\dagger c_{n+1,A} + t_3(n) c_{n,A}^\dagger c_{n+1,B} + t_4(n) c_{n,B}^\dagger c_{n+2,A} + H.c. \right), \quad (5)$$

where,  $t_1(n) = t_1 \left( \frac{2n-1}{2N-1} \right)^\sigma$ ,  $t_2(n) = t_2 \left( \frac{2n}{2N-1} \right)^\sigma$  are the nearest neighbor intracellular and intercellular position-dependent hoppings, and,  $t_3(n) = t_3 \left( \frac{2n-1}{2N-1} \right)^\sigma$ ,  $t_4(n) = t_4 \left( \frac{2n}{2N-1} \right)^\sigma$ . For  $\sigma = 0$ , the Hamiltonian will have translational invariance. Hence, it can be fourier transformed to momentum  $k$  space, where the winding number transition can happen when the components of the bloch vector becomes zero, i.e.,  $d_x(k) = t_1 + (t_2 + t_3) \cos k + t_4 \cos 2k$  and,  $d_y(k) = (t_2 - t_3) \sin k + t_4 \sin 2k$  both becomes 0, which gives us conditions:  $(t_1 + t_2 + t_3 + t_4 = 0)$ ,  $(t_1 - (t_2 + t_3) + t_4 = 0)$ , and,  $(t_1 = t_4$  and  $t_2 = t_3)$  at  $k = 0, \pi$  and  $\pi/2$ , respectively, where we can observe winding number transitions.

## III. WAVE-PACKET VS SEMICLASSICAL DYNAMICS

The first question we try to address here is whether we see any event horizon physics for the Hamiltonian Eq. (4).



0.2

FIG. 1: Time evolution of Gaussian wave packet in the CST-SSH Hamiltonian of system size  $2N = 1000$  (500 unit cells): (a)  $t_1 = t_2 = 1, \sigma = 1, \omega = 25, x_0 = 750, p_0 = -\frac{\pi}{2}$ , the wave packet experiences an eternal slowdown as it approaches the origin; (b)  $t_1 = 1, t_2 = 1.9, \sigma = 1, \omega = 25, x_0 = 750, p_0 = -\frac{\pi}{2}$ , the wave-packet turns back before the origin; (c) peak position of the Gaussian wave packet vs. time for different  $p_0$ , at  $\sigma = 1$ , having  $(t_1, t_2) = (1, 1.9)$ ; (d) peak position vs. time for different  $t_1/t_2$  ratios at  $p_0 = -\frac{\pi}{2}$ . Dotted lines are numerical; solid lines are semiclassical predictions.

Hence, we first study the wave-packet dynamics. In this section, we study the wave packet dynamics under the CST-SSH Hamiltonian of a Gaussian wave packet and compare the results with the semiclassical set of coupled differential equations that govern wave packet trajectories. We consider the following Gaussian wave packet,

$$\psi(x, \tau = 0) = \frac{1}{\sqrt[4]{\pi\omega^2}} e^{-\frac{1}{2}\left(\frac{x-x_0}{\omega}\right)^2} e^{ip_0x}, \quad (6)$$

which describes a normalized gaussian wave packet at time  $\tau = 0$  centered at position  $x_0$  of the lattice, and having initial momentum of  $p_0$ ,  $\omega$  is the width of the wave packet. We find that if  $t_1 \neq t_2$ , the wave-packet first propagates towards an edge and then returns from some point  $x_{min}$ , which we identify as a ‘turning point’. This  $x_{min}$  depends on the details, e.g., initial momentum  $p_0$ , the Hamiltonian parameters  $\sigma$ ,  $t_1$ , and  $t_2$  (see Fig. 1b). On the other hand, for  $t_1 = t_2$  and  $p_0 = -\pi/2$ ,

it eternally slows down while evolving as it approaches the edge  $x = 0$ , and never returns as shown in Fig. 1a. We can identify it as the asymptotic localization of wave packets at the origin, which mimics the key feature expected for wave packet dynamics in the presence of a horizon.

We can dive deeper into the time evolution of the wave packet by obtaining the semiclassical trajectories of the Hamiltonian. For a position-dependent SSH model, the two recursive energy eigenvalue equations can be written as,

$$t_2(n-1)\psi_{B,n-1} + t_1(n)\psi_{B,n} = \epsilon\psi_{A,n} \quad (7)$$

$$t_1(n)\psi_{A,n} + t_2(n)\psi_{A,n+1} = \epsilon\psi_{B,n} \quad (8)$$

Following the reference [46], we introduce continuous function  $\tilde{\psi}_{A/B}(x_n)$  which is related to the discrete  $\psi_{A/B,n}$  of the lattice model as:  $\tilde{\psi}_{A/B}(x_n) = \psi_{A/B,n}$ , where,  $x_n = \frac{n}{N-1}$  is

the position of the  $n$ -th unit cell in the conituum space, with  $\tilde{\Psi}_A(x_n) - \tilde{\Psi}_B(x_n) = \delta x = \frac{1}{2N-1}$ , the minimum distance on the lattice. Expanding the wave functions in Taylor series, we get a mapping between the discrete  $\Psi_{A/B,n\pm 1}$  with continuous  $\tilde{\Psi}_{A/B}(x_n)$  as  $\Psi_{A/B,n\pm 1} = e^{\pm i 2\delta x \hat{p}} \tilde{\Psi}_{A/B}(x_n)$ . The factor of two comes as changing the unit cell from  $n$  to  $n \pm 1$  corresponds to moving  $2\delta x$  in space to the right or left, and the minimum length scale on the lattice is  $\delta x$ . We then end up with the following pairs of equations,

$$\left( t_2(\hat{x} - 2\delta x) e^{-2i\delta x \hat{p}} + t_1(\hat{x}) \right) \tilde{\Psi}_B(x, \tau) = i\partial_\tau \tilde{\Psi}_A(x, \tau) \quad (9)$$

and,

$$\left( t_1(\hat{x}) + t_2(\hat{x}) e^{2i\delta x \hat{p}} \right) \tilde{\Psi}_A(x, \tau) = i\partial_\tau \tilde{\Psi}_B(x, \tau), \quad (10)$$

where,  $\tilde{\Psi}_{A/B}(x, \tau) = \tilde{\Psi}_{A/B}(x) e^{-i\epsilon\tau}$ . Combining the two equations, we get the continuum Hamiltonian as a  $2 \times 2$  matrix,

$$\tilde{H} = \begin{pmatrix} 0 & t_1(\hat{x}) + e^{-2i\delta x \hat{p}} t_2(\hat{x}) \\ t_1(\hat{x}) + t_2(\hat{x}) e^{2i\delta x \hat{p}} & 0 \end{pmatrix},$$

which acts on the spinor  $\Psi(x, \tau) = \begin{pmatrix} \tilde{\Psi}_A(x, \tau) \\ \tilde{\Psi}_B(x, \tau) \end{pmatrix}$ . Now, neglecting the commutation relation between  $\hat{x}$  and  $\hat{p}$ , and then, rescaling the momentum and time as  $p \rightarrow p/\delta x$  and  $\tau \rightarrow \tau/\delta x$ , we could express the energy as follows, and with it, we can obtain the equation of motion. The semiclassical equations of motion (in one dimension) read:

$$\dot{x} = \frac{\partial E_\pm}{\partial p}, \quad \dot{p} = -\frac{\partial E_\pm}{\partial x}, \quad (11)$$

where,

$$E_\pm(x, p) = \pm \sqrt{t_1^2(x) + t_2^2(x) + 2t_1(x)t_2(x) \cos(2p)} \quad (12)$$

is the energy expression, and correspondingly, one can obtain equations of motion as,

$$\dot{x} = \frac{\partial E_\pm}{\partial p} = \mp \frac{2t_1(x)t_2(x) \sin(2p)}{\sqrt{t_1^2(x) + t_2^2(x) + 2t_1(x)t_2(x) \cos(2p)}} \quad (13)$$

$$\begin{aligned} \dot{p} &= -\frac{\partial E_\pm}{\partial x} \\ &= \mp \frac{t_1(x)t_1'(x) + t_2(x)t_2'(x) + \cos(2p)(t_1'(x)t_2(x) + t_1(x)t_2'(x))}{\sqrt{t_1^2(x) + t_2^2(x) + 2t_1(x)t_2(x) \cos(2p)}} \end{aligned} \quad (14)$$

Solving these two coupled differential equations, one can easily obtain the semiclassical trajectories. Here, the  $\mp$  signs just indicate the direction of the propagation of the trajectories. In figure 1c and 1d, the semi-classical trajectories are compared with the peak position of exact dynamics results. The results show extraordinary agreement. Moreover, the

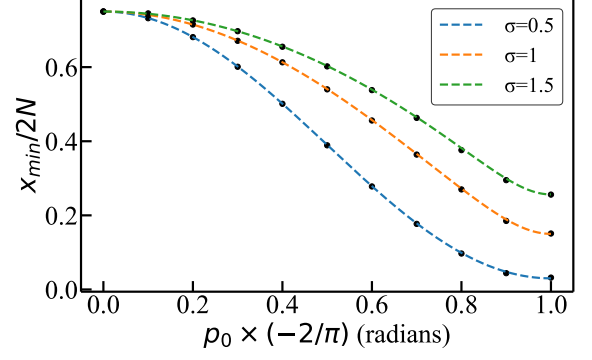


FIG. 2: For the CST-SSH model having system size  $2N = 1000$  (500 unit cells),  $t_1 = 1, t_2 = 1.5$ , plotting of turning point by numerical calculation (black dotted lines) and from semiclassical formula 17 (colored dashed lines) at different initial momenta  $p_0$  for different values of  $\sigma$

semiclassical result can also mimic the event horizon physics for  $t_1 = t_2$  and  $p_0 = -\pi/2$ .

Semiclassical trajectories can also allow us to predict the turning point for  $p_0 \neq -\pi/2$ . One can analytically obtain the turning point by taking the conserved nature of the average energy of wave packet from the semiclassical calculation. From equation 12, one obtains,

$$\begin{aligned} E^2(x, p) &= E_0^2(x_0, p_0) = t_1^2(x) + t_2^2(x) + 2t_1(x)t_2(x) \cos(2p) \\ \implies \cos(2p) &= \frac{E_0^2 - (t_1^2(x) + t_2^2(x))}{2t_1(x)t_2(x)}. \end{aligned} \quad (15)$$

Now, at the turning point  $(x_{\min}, t_{\min})$ ,  $\dot{x} = 0$ , which implies  $p = 0$ , substituting which in Eq. 15, one gets,

$$E_0 = t_1(x_{\min}) + t_2(x_{\min}) \quad (16)$$

with the position dependent hoppings  $t_1(x_{\min}) \sim t_1 x_{\min}^\sigma$  and  $t_2(x_{\min}) \sim t_2 x_{\min}^\sigma$ . The Eq. 16 can be simplified to obtain the  $x_{\min}$  expression as,

$$x_{\min} = x_0 \left[ \frac{t_1^2 + t_2^2 + 2t_1 t_2 \cos(2p_0)}{(t_1 + t_2)^2} \right]^{\frac{1}{2\sigma}} \quad (17)$$

Figure. 2 shows how the turning point varies with different  $p_0$  values at different  $\sigma$ . The numerical and analytical turning points are extremely well lined up, solidifying the validity of semiclassical calculations. Moreover, the equation suggests that for  $x_{\min}$  to be zero, the two hopping  $t_1$  and  $t_2$  must be equal, leading to a more simplified expression  $x_{\min} = x_0 (\cos p)^{\frac{1}{\sigma}}$ , when  $p = \pm\pi/2$ , only then  $x_{\min}$  becomes 0. Hence, in the case of  $t_1 \neq t_2$ , the wave packet has no initial momentum  $p_0$  value for which the turning point becomes 0. It also validates our previous numerical finding, i.e., only when  $t_1 = t_2$ , the model can show the synthetic horizon effect, and that too for  $p_0 = -\pi/2$ , which also has been observed for the tight binding lattice model [22, 25, 46].

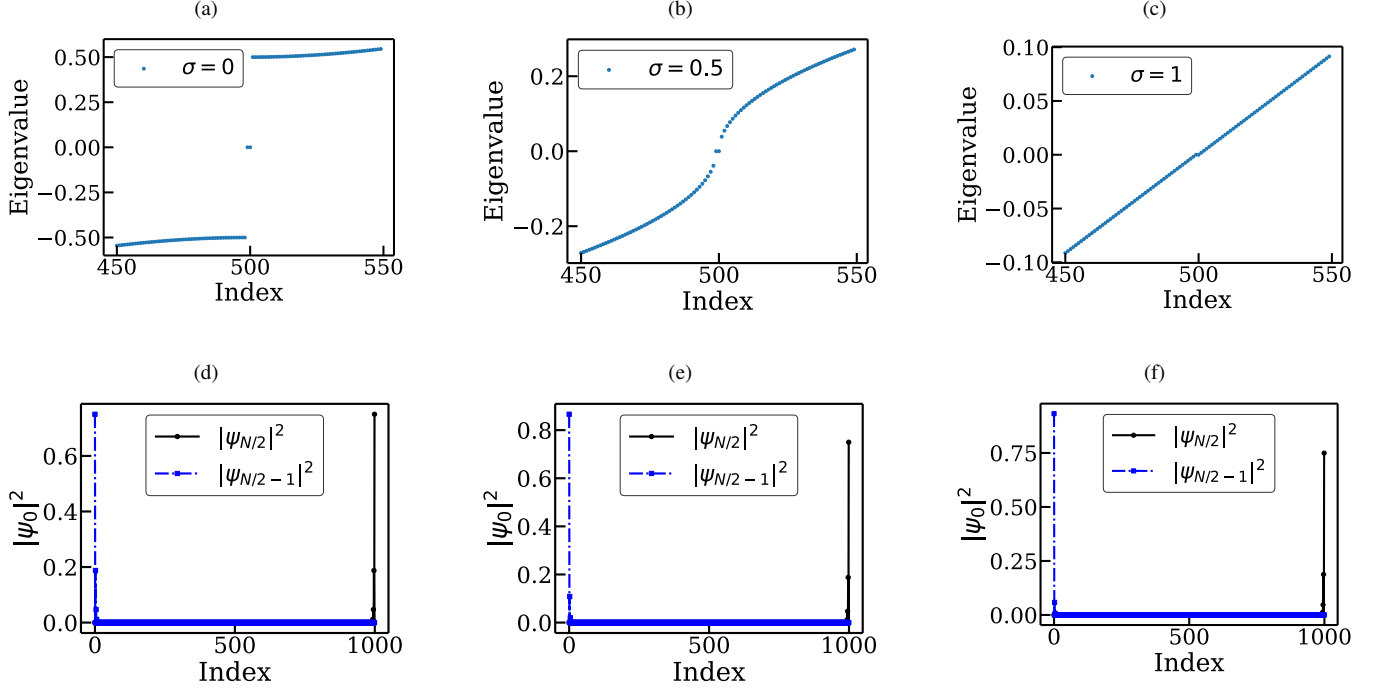


FIG. 3: Closing of the energy band gap and variation of zero energy eigen states variation with  $\sigma$ : for a CST-SSH model having system size  $2N = 1000$  (500 unit cells) with  $t_1 = 0.5$  and  $t_2 = 1$ . Top row (a)–(c): Eigenvalue spectra for  $\sigma = 0, 0.5$ , and 1 respectively. Bottom row (d)–(f): Corresponding zero-energy eigenstates profiles.

#### IV. ANALYTICAL EXPRESSION FOR THE EXACT ZERO ENERGY EIGENFUNCTIONS

From the wave-packet dynamics, it is apparent that the CST SSH model can also mimic horizon physics. The next question is, does this model show a topological phase transition? Note that in the  $\sigma = 0$  limit, this model is identical to the usual SSH model and shows a topological phase transition when  $t_1 = t_2$  between topologically trivial phase ( $t_1 > t_2$ ) and topologically non-trivial phase ( $t_2 > t_1$ ). The consequence of the topologically non-trivial phase is that for  $t_2 > t_1$ , the Hamiltonian  $H$  (4) under open-boundary conditions has two zero-energy states, and they are localized at the two edges. Now, the automatic question arises, what will happen to the fate of those edge states for  $\sigma > 0$ , will such edge states survive? First, we perform a numerical check in Fig. 3. Figures in the upper panel suggest that zero energy states still survive for finite  $\sigma$ , though the gap is becoming smaller with increasing  $\sigma$ . Moreover, those states remain localized at the edges. However, unlike the usual SSH model, the states are asymmetric; the left edge state seems to become more localized compared to the right edge state with increasing  $\sigma$ .

It is reasonably straightforward to obtain those zero eigenstates by solving the time-independent Schrödinger equation for the Hamiltonian (4), and one can easily obtain two recursive relations for two sub-lattices A and B.

For sublattice A:

$$t_2(n-1)\psi_{B,n-1} + t_1(n)\psi_{B,n} = 0 \quad (18)$$

For sublattice B:

$$t_1(n)\psi_{A,n} + t_2(n)\psi_{A,n+1} = 0 \quad (19)$$

Now, from (18),

$$\begin{aligned} \psi_{B,n} &= -\frac{t_1(n+1)}{t_2(n)}\psi_{B,n+1} \\ &= \left(-\frac{t_1(n+1)}{t_2(n)}\right)\left(-\frac{t_1(n+2)}{t_2(n+1)}\right)\cdots\left(-\frac{t_1(N)}{t_2(N-1)}\right)\psi_{B,N} \\ &= \left(-\frac{t_1}{t_2}\right)^{N-n}\prod_{m=n+1}^N\left(\frac{2m-1}{2(m-1)}\right)^\sigma\psi_{B,N} \end{aligned} \quad (20)$$

Likewise, for sublattice B, we can obtain from (19),

$$\begin{aligned} \psi_{A,n} &= -\frac{t_1(n-1)}{t_2(n-1)}\psi_{A,n-1} \\ &= \left(-\frac{t_1}{t_2}\right)^{n-1}\prod_{m=1}^{n-1}\left(\frac{2m-1}{2m}\right)^\sigma\psi_{A,1} \end{aligned} \quad (21)$$

These two zero-energy eigenstates  $\psi_{A,n}$  and  $\psi_{B,n}$  will appear on the left and right edges of the chain, respectively.  $\psi_{B,N}$

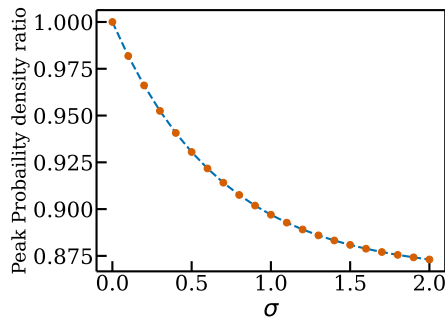


FIG. 4: for  $t_1 = 0.5, t_2 = 1$ , ratio of right-to-left peak of probability densities vs  $\sigma$  for system size  $2N = 1000$  (500 unit cells). Here the dotted lines represent the numerical calculations and the dashed lines are from the analytical expressions of the zero energy eigenstates 21,20

and  $\psi_{A,1}$  can easily be obtained by normalizing the eigen states. For the standard SSH model, with  $\sigma = 0$ , both states are identical, only one is peaked at the left edge, and the other at the right. But with the introduction of  $\sigma$ , asymmetry arises. The state on the right edge remains almost the same for non-zero  $\sigma$ , and the peak height on the left edge keeps increasing with  $\sigma$ . Figure. 4 shows how the right-to-left peak ratio of probability densities varies with  $\sigma$ , showing exact matching with the ratio calculation from the analytical expression.

Another thing to note is the closing of the energy gap with  $\sigma$ . We observe that the gap gradually closes with increasing  $\sigma$  and becomes almost non-existent as  $\sigma$  reaches 1. From Fig. 5, we observed that  $\Delta E$  decreases with  $\sigma$  as  $\Delta E \propto N^{-\sigma}$  for a given fixed  $t_1$  and  $t_2$ . Note that the finite-size system on the lattice will always have a gap, and a typical gap between two adjacent energy eigenvalues decreases with system size as  $N^{-1}$  (we have found the same for our model as well). Thus, the ratio between  $\Delta E$  and the typical gap in the spectrum scales as  $N^{1-\sigma}$ , indicating the presence of isolated zero-energy states even for non-zero  $\sigma < 1$ . The fact that  $N\Delta E$  increases with  $N$ , suggests the system remains gapped even in the thermodynamic limit for  $\sigma < 1$  [49]. Nevertheless, we also observe well-localized zero-energy edge states for the  $\sigma$  higher than 1 as well. This can be attributed to the robustness of the system's topology.

## V. TOPOLOGICAL SIGNATURES

In the previous section, the survival of the zero-energy edge states for  $\sigma > 0$  shows a signature that the CST-SSH Hamiltonian can also host the topologically non-trivial phase. In order to become more certain, one needs to understand the symmetries of the model, as well as some proper topological markers, which are required. First, we investigate whether even after the introduction of warping of spacetime ( $\sigma$ ), the Hamiltonian will still remain in the BDI category with winding number as its topological invariant quantity, as it is observed for the usual

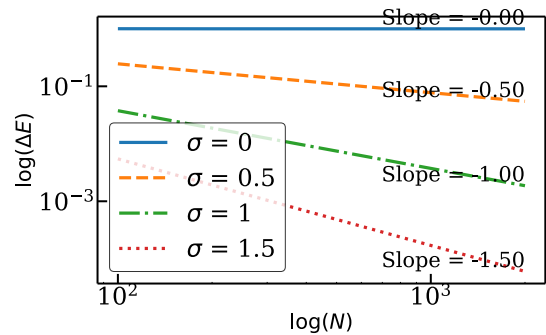


FIG. 5: for  $t_1 = 0.5, t_2 = 1$  energy gap  $\Delta E$  at various system size  $N$  for different  $\sigma$

SSH model. Since the two position-dependent hopping terms  $t_1(n)$  and  $t_2(n)$  are real, the time reversal operator acting on the Hamiltonian  $\hat{T}H\hat{T}^{-1} = H$  leaves it invariant. Moreover, the Hamiltonian being a spinless fermionic system,  $\hat{T}^2 = \mathbb{I}$ . For chiral symmetry, first, we define  $\hat{\Gamma}_A = \sum_{n=1}^N c_{n,A}^\dagger c_{n,A}$  and  $\hat{\Gamma}_B = \sum_{n=1}^N c_{n,B}^\dagger c_{n,B}$  as projectors on sublattice A and B [50]. Then, the chiral operator is defined by  $\hat{\Gamma} = \hat{\Gamma}_A - \hat{\Gamma}_B$ , which anti-commutes with the Hamiltonian  $\hat{\Gamma}H\hat{\Gamma} = -H$ , since the bipartite nature is maintained in the modified position-dependent SSH model. This anti-commutation relation holds regardless of the position-dependent nature of the hopping amplitudes [50]. Time reversal and Chiral symmetry being present with  $T^2 = \Gamma^2 = \mathbb{I}$ , we can combine them as,  $\hat{C} = \hat{T}\hat{\Gamma}$ , which can act as a particle hole symmetry, i.e., an anti-unitary operator that anti-commutes with the Hamiltonian, and also  $\hat{C}^2 = \mathbb{I}$ . Thus, this CST-SSH Hamiltonian remains in the BDI category in the Altland-Zirnbauer tenfold classification of topological insulators and superconductors [51, 52] with an integer  $\mathbb{Z}$  topological invariant like its standard counterpart in the usual SSH model. So, the symmetries remain invariant under the position-dependent hopping amplitude, and so does the topological invariant, i.e., winding number. However, in the CST-SSH model, the absence of translational symmetry prevents us from utilizing the k-space to calculate the winding number. Therefore, we adopt two real space markers to calculate the topological invariants: (i) Local topological marker (LTM), (ii) Mean chiral displacement (MCD).

### A. Local Topological Marker

For a dimer chain with broken translational symmetry, the Local Topological Marker (LTM) can give the value of the topological invariant quantity in its bulk. We here obtain the winding number in real space using LTM [53, 54]. It is based on the rearranged eigenfunctions corresponding to the ascending eigenvalues. The Local topological Marker(LCM) can be

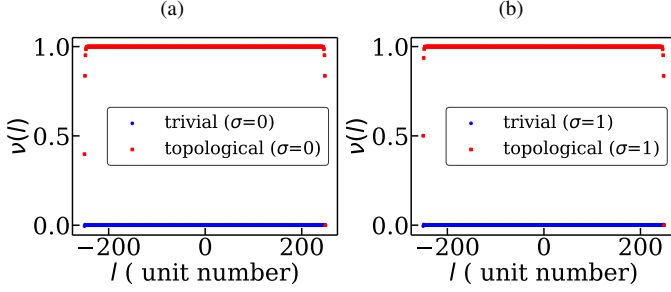


FIG. 6: Local Topological Marker (LTM) for (a)  $\sigma = 0$  and, (b)  $\sigma = 1$  for trivial  $(t_1, t_2) = (1, 0.5)$  and topological phase  $(t_1, t_2) = (0.5, 1)$ , for the CST-SSH model having system size  $2N = 1000$  (500 unit cells)

defined as:

$$v(l) = \frac{1}{2} \sum_{a=A,B} \{ (\mathbb{Q}_{BA}[\mathbb{X}, \mathbb{Q}_{AB}])_{la,la} + (\mathbb{Q}_{AB}[\mathbb{Q}_{BA}, \mathbb{X}])_{la,la} \}, \quad (22)$$

Here,  $\mathbb{X}$  is the position operator.  $\mathbb{Q}$  can be defined from the modal matrix  $\mathbb{U}$ , which is comprised of all the normalized eigen vectors with ascending order, explicitly,  $\mathbb{U} = [\mathbf{U}_1, \mathbf{U}_2, \dots, \mathbf{U}_n, \mathbf{U}_{n+1}, \dots, \mathbf{U}_N]$ . Here,  $\mathbb{U}_- = [\mathbf{U}_1, \mathbf{U}_2, \dots, \mathbf{U}_n]$ , and  $\mathbb{U}_+ = [\mathbf{U}_{n+1}, \mathbf{U}_{n+2}, \dots, \mathbf{U}_N]$  are corresponds to below and above the band gap energy spectrum. Then one can define the projectors as  $\mathbb{P}_- = \mathbb{U}_- \mathbb{U}_-^T$  and  $\mathbb{P}_+ = \mathbb{U}_+ \mathbb{U}_+^T$ , and  $\mathbb{Q}$  as,  $\mathbb{Q} = \mathbb{P}_+ - \mathbb{P}_-$ , which further can be decomposed as,  $\mathbb{Q} = \mathbb{Q}_{AB} + \mathbb{Q}_{BA} = \Gamma_A \mathbb{Q} \Gamma_B + \Gamma_B \mathbb{Q} \Gamma_A$ , where  $\Gamma = \Gamma_A - \Gamma_B$  is the chiral operator. More about the formula and the operators can be found in the appendix of [53, 54]. From the figure 6, we observe that even for  $\sigma = 1$ , the LTM shows the same winding number for the CST-SSH Hamiltonian as its usual SSH counterpart. While  $t_2 > t_1$ , the LTM shows  $v = 1$ , indicating topologically non-trivial phase, and for  $t_1 > t_2$ ,  $v = 0$  signifying the trivial phase. There is no apparent difference between the standard and the position-dependent hopping SSH model for this static marker.

### B. Mean Chiral Displacement

The previous topological measure was a static measure; in this section, we use a dynamical topological measure, which we call Mean Chiral Displacement (MCD) [53, 55], can be used to detect the winding number. The MCD is defined as [],

$$C(\tau) = 2 \langle \psi(\tau) | \Gamma \mathbb{X} | \psi(\tau) \rangle, \quad (23)$$

where  $|\psi(\tau)\rangle = e^{-iH\tau} |\psi_i\rangle$ , i.e.,  $|\psi(\tau)\rangle$  is the time evolved state of an initially localized state at  $n = N/2$  unit cell in the A sublattice, i.e.,  $|\psi_i\rangle$ .  $\Gamma$ ,  $\mathbb{X}$  are chiral and displacement operators, respectively. In the figure 11, we show the time-dependent MCD for both the trivial and topological phases, where it oscillates and converges to 0 in the case of a trivial phase and, on the other hand, saturates to 1 in the case of a

topological phase for the usual SSH model. On the other hand, for  $\sigma \neq 0$  also, the MCD oscillates around its respective winding number, but the fluctuations are much higher compared to  $\sigma = 0$ , though the average MCD remains the same. We, then, measure the fluctuation by computing the long-time variance of the MCD for different  $\sigma$ . Interestingly, we observe that this fluctuation is at most when  $\sigma = 1$ . Figure. 7c shows that with increasing system size, fluctuation for a particular  $\sigma$  increases, and, for a particular system size, it is maximum around  $\sigma = 1$ . Overall, the MCD results complement our previous results for the static measure. This indeed proves that, like the usual SSH model, even the CST-SSH model displays two topologically distinct phases corresponding to winding numbers 0 (when  $t_2/t_1 < 1$ ) and 1 (when  $t_2/t_1 > 1$ ).

## VI. QUENCH DYNAMICS: FROM TOPOLOGICAL TO TRIVIAL PHASE

In this section, we study the quench dynamics across the topological transition point. We prepare our initial state  $|\psi_i\rangle$  as one of the zero-energy eigenstates of the CST-SSH Hamiltonian for  $t_2 > t_1$ . Note, this is the topologically non-trivial phase, having two edge modes. Then, we quench across the transition point in the topologically trivial phase. It implies  $t_2 < t_1$  for the post-quench Hamiltonian, which we identify as  $H_f$ . The survival probability of the initial state after quench is given by [56, 57],

$$P_i(\tau) = |\langle \psi_i | e^{-iH_f \tau} | \psi_i \rangle|^2. \quad (24)$$

It is basically a measurement of the likelihood of the zero-energy eigenstate of a topologically nontrivial Hamiltonian remaining the same after the unitary time evolution of the state in another Hamiltonian with winding number 0. Figure. 8 shows the variation of the survival probability with time for the usual SSH model, i.e.,  $\sigma = 0$ , and for the CST-SSH model with  $\sigma = 0.5$ . We quench from  $(t_1, t_2) = (0.5, 1)$  to  $(t_1, t_2) = (1, 0.5)$ . For the initial state, i.e., localized at the right edge, the time evolution of the survival probability is almost identical for the usual SSH and the CST-SSH model (see Fig. 8a). The survival probability goes to zero reasonably quickly. However, the dynamics are quite different between these two models for the left edge mode (see Fig. 8b). While for the usual SSH, the dynamic is almost indistinguishable from that obtained for the right edge mode, for  $\sigma > 0$ , the survival probability seems to oscillate between 0 and 1 for the CST-SSH model. We find that the oscillation period increases with increasing  $\sigma$ . The fact that dynamics is identical for usual SSH and not for CST-SSH is not too surprising, given that we found in Sec. IV that both edge states are symmetric for  $\sigma = 0$ , and asymmetry kicks in as soon as  $\sigma > 0$ . However, it still does not explain why the survival probability of the left-edge states oscillates. Hence, we plot the absolute value of the time-evolved wavefunction in Fig. 9, and find that for the CST-SSH model, while under time evolution, the right edge state moves toward the other side of the lattice, while the left edge mode kind of remains there. If one tracks the peak position, one finds that it moves a bit to the right and then

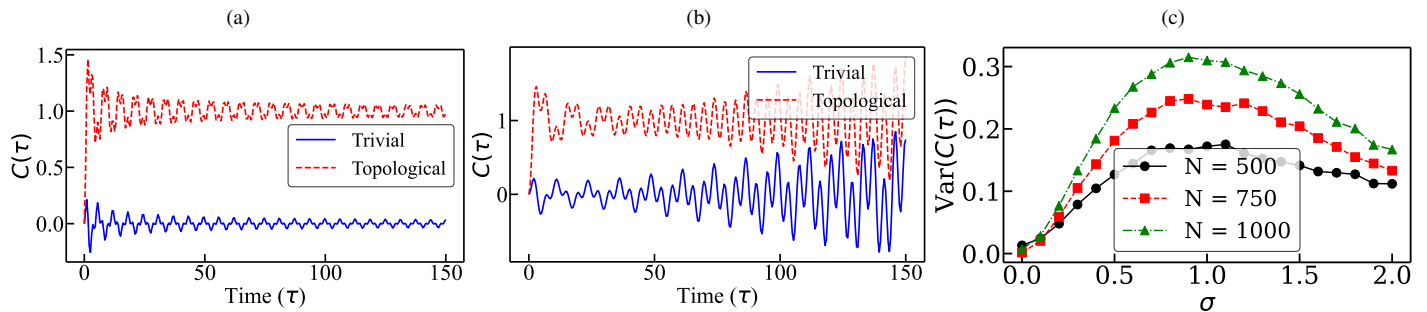


FIG. 7: (a),(b): Time dependent MCD for both topological (red) with  $(t_1, t_2) = (0.5, 1)$  and trivial (blue) with  $(t_1, t_2) = (1, 0.5)$  for (a)  $\sigma = 0$  and, (b)  $\sigma = 1$  for the CST-SSH model having system size  $2N = 1000$  (500 unit cells), (c) Fluctuation measurement as  $\text{Var}(C(t))$  vs  $\sigma$  for different system sizes  $N$

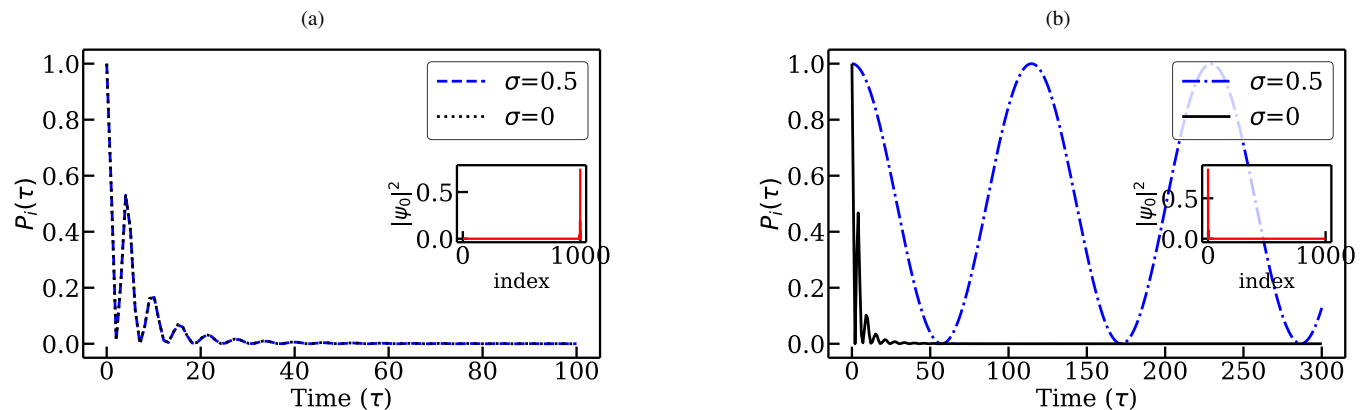


FIG. 8: Measurement of survival probability  $P_i(t)$  from winding number 1 (with  $(t_1, t_2) = (0.5, 1)$ ) to winding number 0 (with  $(t_1, t_2) = (1, 0.5)$ ) for (a) right edge zero energy eigen state and, (b) left edge zero energy eigen state, for the CST-SSH model having system size  $2N = 1000$  (500 unit cells)

again comes back, keeping up this to-and-fro motion. This is precisely what gets manifested in the survival probability plot. Moreover, we find the same picture even when solving the semi-classical equation of motion (see inset of Fig. 9).

## VII. EXTENDED CST-SSH MODEL

In this section, we consider an extended version of the SSH model, described by the Hamiltonian 5. Here, this system can possess a winding number ranging from  $-1$  to  $2$ . Such models can host more than one edge mode on each lattice edge (see Appendix A). While in the case of the CST-SSH model, the winding numbers of the distinct topological phases were either  $\nu = 0$  (topologically trivial) or  $\nu = 1$ . By choosing suitable parameters, one can have even topological phases with a higher winding number in case of the Hamiltonian extended CST-SSH model in Eq.5. First, we consider  $t_3 = t_4 = 0$ , and in this limit for the Hamiltonian  $H_{ext}$ , we have also calcu-

lated the local topological marker (LTM) and find in case of both  $\sigma = 0$  and  $1$ , the winding numbers are  $\nu = 0$  and  $1$  for  $(t_1, t_2) = (1, 0.5)$ ,  $(0.5, 1)$ , respectively. Likewise, for parameters  $(t_1, t_2, t_3, t_4) = (0.5, 0, 1, 0)$ ,  $(0, 1, 1, -3)$ , one obtains winding number  $\nu = -1, 2$ , respectively for both  $\sigma = 0$  and  $\sigma = 1$  (see Fig. 10). These results show that topological features in the CST version of the SSH type models survive even for the extended CST-SSH model. Thus, we can say that the two gap-closing constraints also remain the same for the extended CST-SSH model.

In this extended CST-SSH model, we can see clear winding number transition points. For example,  $(t_1, t_2, t_3, t_4) = (3, -2, 1, -4)$  is a transition point between  $\nu = 1$  to  $\nu = 2$  phase provided we keep  $t_1, t_2, t_3$  fixed and vary  $t_4$ . If we allow  $t_4$  to go slightly below  $-4$ , while keeping the other parameters the same, the winding number becomes  $2$ , and if one allows  $t_4$  to go higher than  $-2$ , it will make the winding number  $1$ ; making the particular combination of hoppings a transition point. If we study a Gaussian wavepacket evolution in this ex-

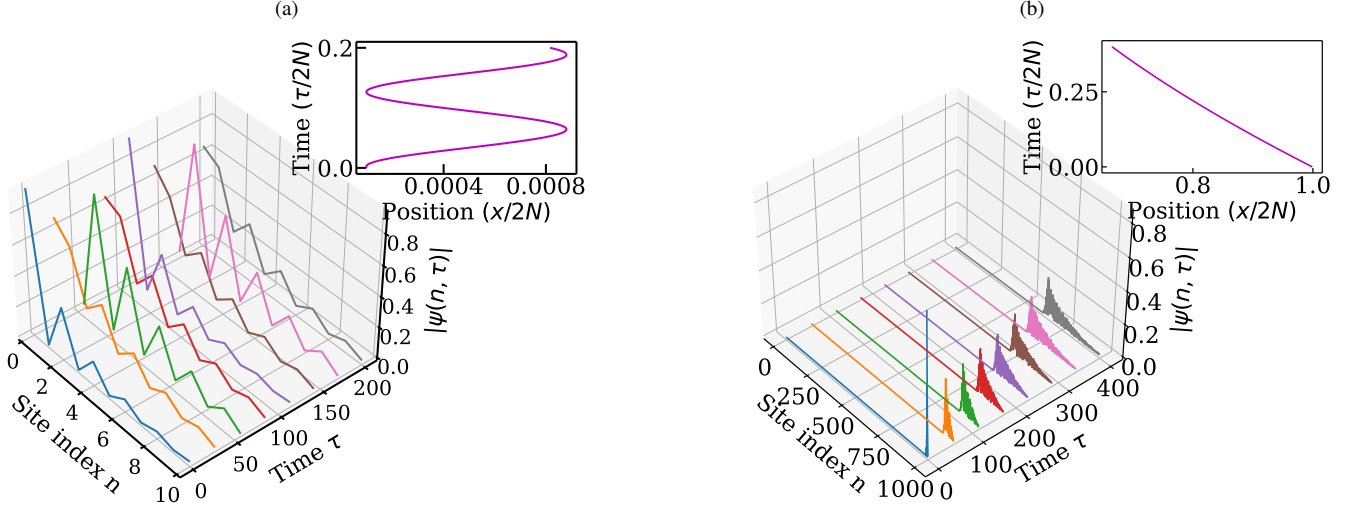


FIG. 9: For the CST-SSH model having system size  $2N = 1000$  (500 unit cells), Time evolution of the zero energy eigenstates: (a) left, and, (b) right edge zero energy eigenstate of a Hamiltonian with winding number 1, in another Hamiltonian with winding number zero. Inset of Fig. (a) shows the semiclassical dynamics near the origin, where the left edge state is located. Inset of Fig. (b) shows the semiclassical dynamics where the right edge state is located.

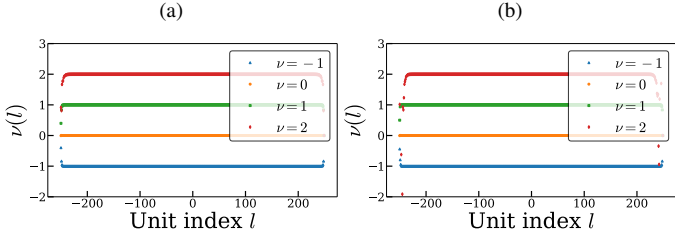


FIG. 10: Local Topological Marker (LTM) for extended CST-SSH model (a)  $\sigma = 0$  and (b)  $\sigma = 1$ , for the CST-SSH model having system size  $2N = 1000$  (500 unit cells), giving the same winding numbers for both  $\sigma$  values.  $(t_1, t_2, t_3, t_4) = (0.5, 0, 1, 0), (1, 0.5, 0, 0), (0.5, 1, 0, 0), (0, 1, 1, -3)$  are chosen to obtain winding numbers  $-1, 0, 1, 2$ , respectively.

tended CST-SSH Hamiltonian for this particular topological transition point, we observe, in a similar manner, an eternal slowdown of the wavepacket for  $\sigma > 0$ , for initial wavepacket momentum  $|p_0| = \frac{\pi}{2}$  (see Fig.11a). Figure. 11b also shows that for another transition point obeying  $t_1 + t_2 + t_3 + t_4 = 0$  with  $(t_1, t_2, t_3, t_4) = (0, 1, 1, -2)$ , also shows critical slowdown for  $|p_0| = \pi$ . For other than transition points, the wavepacket returns before reaching the origin (see Fig.11c). Similar behavior can be observed for other transition points, like from  $\nu = 0$  to  $\nu = 1$ , from  $\nu = 0$  to  $\nu = -1$ , from  $\nu = 0$  to  $\nu = 2$  etc. Thus, these observations imply the presence of a synthetic horizon at the topological phase-transition points, and that strengthens our claims that horizon physics emerges only at the topological transition points in these models.

#### A. Semiclassical dynamics for the Extended CST-SSH model

In a similar spirit to the previous section. III, we can analyze the semiclassical dynamics for the extended version of the CST-SSH model. Since here we have two additional hoppings, in our recurring relation, we will have two more variables. The two relations will be:

$$t_4(n-2)\psi_{B,n-2} + t_2(n-1)\psi_{B,n-1} + t_1(n)\psi_{B,n} + t_3(n)\psi_{B,n+1} = \epsilon\psi_{A,n} \quad (25)$$

$$t_3(n-1)\psi_{A,n-1} + t_1(n)\psi_{A,n} + t_2(n)\psi_{A,n+1} + t_4(n)\psi_{A,n+2} = \epsilon\psi_{B,n} \quad (26)$$

Now, we, in a similar manner, after introducing the continuous function  $\tilde{\Psi}_{A/B}(x_n)$ , and expanding it in Taylor series, can obtain the continuum Hamiltonian, and then similarly the semiclassical equations of motion:

$$\tilde{H}_{ext} = \begin{pmatrix} 0 & T(\hat{x}, \hat{p}) \\ T^*(\hat{x}, \hat{p}) & 0 \end{pmatrix},$$

where,  $T(\hat{x}, \hat{p}) = t_1(\hat{x}) + e^{-2i\delta x \hat{p}} t_2(\hat{x}) + t_3(\hat{x}) e^{2i\delta x \hat{p}} + e^{-4i\delta x \hat{p}} t_4(\hat{x})$ , and the semiclassical equations of motion,

$$\dot{x} = \frac{\partial E_{\pm}}{\partial p}, \quad \dot{p} = -\frac{\partial E_{\pm}}{\partial x}. \quad (27)$$

Here, The energy expression,

$$E_{\pm}(x, p) = \pm |T(x, p)| = \pm \sqrt{T_R^2(x, p) + T_I^2(x, p)}$$

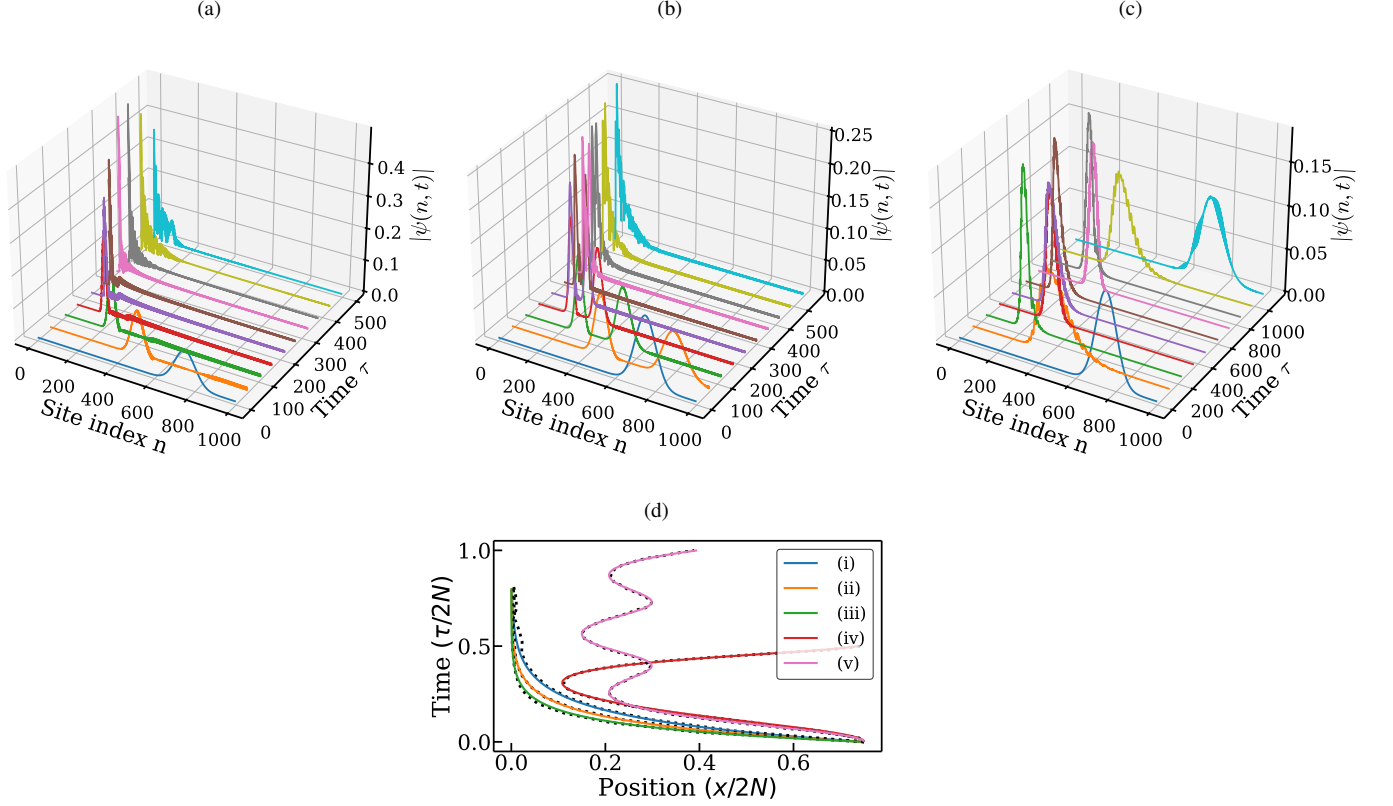


FIG. 11: Time evolution of Gaussian wave packet in the Extended CST-SSH Hamiltonian of system size  $2N = 1000$  (500 unit cells) with  $\sigma = 1$ ,  $\omega = 50$ ,  $x_0 = 750$ : (a) obeying the relation  $t_1 - (t_2 + t_3) + t_4 = 0$  with hopping  $(t_1, t_2, t_3, t_4) = (3, -2, 1, -4)$ , with  $|p_0| = \pi/2$ , (b) obeying the relation  $t_1 + t_2 + t_3 + t_4 = 0$  with hopping  $(t_1, t_2, t_3, t_4) = (0, 1, 1, -2)$ , at  $|p_0| = \pi$  (c) extended CST-SSH having winding no 2, with hopping parameters  $(t_1, t_2, t_3, t_4) = (0, 1, 1, -3)$  at  $|p_0| = \pi$  (d) peak position vs. time for different combinations of hopping and initial momentum  $(t_1, t_2, t_3, t_4, p_0)$ : (i)  $(0, 1, 1, -2, \pi)$ , (ii)  $(3, -2, 1, -4, \pi/2)$ , (iii)  $(3, 1, 1, 3, \pi/4)$  (iv)  $(3, -2, 1, -3, \pi/2)$ , and, (v)  $(0, 1, 1, -3, \pi)$ . (i), (ii) and (iii) suffer eternal slowdown; whereas, (iv) and (v) return before reaching the origin. Dotted black lines are numerical; solid colored lines are semiclassical predictions.

, where,  $T_R = t_1(x) + (t_2(x) + t_3(x))\cos(2p) + t_4(x)\cos(4p)$  and  $T_I(x, p) = (t_3(x) - t_2(x))\sin(2p) - t_4(x)\sin(4p)$  are the real and imaginary part of  $T(x, p)$ . Now, after substituting the values of  $T_R$  and  $T_I$ , one can obtain the equations of motion as:

$$\dot{x} = \pm \frac{1}{\sqrt{T_R^2(x, p) + T_I^2(x, p)}} (T_R \partial_p T_R + T_I \partial_p T_I) \quad (28)$$

$$\dot{p} = \mp \frac{1}{\sqrt{T_R^2(x, p) + T_I^2(x, p)}} (T_R \partial_x T_R + T_I \partial_x T_I), \quad (29)$$

where,  $\partial_p$  and  $\partial_x$  are the partial derivatives with respect to  $p$  and  $x$ , respectively. Fig. 11d shows the comparison between the numerical time evolution (dotted black lines) and the semiclassical equations of motion (colored lines) to obtain the peak positions of the wave packets at various times for different hopping parameters. The semiclassical calculations show excellent agreement with the numerical time evolution for this extended version as well. One can obtain the analytical value of the turning point following a similar way, by equating the energy expression at  $(x_0, p_0)$  and at  $(x_{\min}, p)$ , where choosing an appropriate  $p$  makes  $\dot{x} = 0$ . For  $p = 0$ , the turning position reads as:

$$x_{\min} = x_0 \left[ \frac{(t_1 + (t_2 + t_3) \cos 2p + t_4 \cos 4p)^2 + ((t_3 - t_2) \sin 2p - t_4 \sin 4p)^2}{(t_1 + t_2 + t_3 + t_4)^2} \right]^{\frac{1}{2\sigma}} \quad (30)$$

This gives us that, when  $t_1 - (t_2 + t_3) + t_4 = 0$ ,  $x_{\min}$  is equal

to 0 at  $|p_0| = \frac{\pi}{2}$ ; and when  $(t_1 - t_4)^2 + (t_3 - t_2)^2 = 0$ ,  $x_{\min} = 0$

at  $|p_0| = \frac{\pi}{4}$ , which are precisely two of the gap closing conditions, i.e., topological transition constraints. One important thing to observe is that when we derived the formula, we already assumed that  $(t_1 + t_2 + t_3 + t_4) \neq 0$ , which prevents us from obtaining the other condition. So, if our Hamiltonian has the hopping parameters  $t_1, t_2, t_3, t_4$  that add to 0, we can not use the formula. In such cases, we go to the next root of  $\sin(2p)$ , which gives us  $\dot{x} = 0$ , which is for  $p = \pi/2$ . Then the  $x_{\min}$  will have  $(t_1 - (t_2 + t_3) + t_4)^2$  in the denominator instead. In this formula,  $x_{\min}$  will be 0 only when  $(t_1 + t_2 + t_3 + t_4) = 0$ , at initial momentum  $|p_0| = \pi$ , which is the other gap closing condition. In case of non-transition points, the minimum of these two would give us the turning point.

Thus, we see that the gap-closing conditions that determine the topological transition between different winding numbers are also conditions for  $x_{\min}$  to become 0. This shows that only at topological transition points, we observe horizon physics at the extended CST-SSH model, which strengthens our findings, discussed in the above sections.

### VIII. SUMMARY AND DISCUSSION

In this paper, we investigate the topological properties of the CST-SSH model. First, we analyze the energy spectrum and find that when the intercell hopping is larger than the intracell hopping, a pair of zero-energy states emerges. These states are localized at the two edges of the lattice. However, unlike in the conventional SSH model, these edge states are not symmetric. We also find that, similar to the usual SSH model, the spectrum exhibits a gap whenever the intra- and inter-cell hopping amplitudes are unequal. However, this gap scales to zero with system size as  $N^{-\sigma}$ . Since the typical gap of a finite-size system scales as  $N^{-1}$ , it implies that for  $\sigma < 1$  the spectrum remains gapped in the thermodynamic limit [49]. Moreover, we use various real-space topological markers, both static and dynamic, which show a clear signature of a topological phase transition between a topologically trivial phase and a non-trivial phase with winding number 1. On the other hand, we find that the physics of the event horizon manifests only at the transition point, where a critical slowdown occurs for zero-energy wave packets near the

boundary. The wave-packet dynamics results are also supported by an analytical calculation of semiclassical trajectories. We have also generalized our results to the extended CST-SSH model, which can support topological phases with higher winding numbers. In this model as well, we demonstrate that the critical slowdown of the wavepacket occurs only at the transition point between two topologically distinct phases. With the advancement of cold-atom experiments, there is potential for our predictions to be verified in the near future [58–60], which could enrich our understanding of both black hole physics and topology.

### ACKNOWLEDGMENTS

R.M. acknowledges the DST-Inspire fellowship by the Department of Science and Technology, Government of India, SERB start-up grant (SRG/2021/002152).

### Appendix A: Zero edge states of the Extended CST-SSH Model

In this section, we discuss both the energy band closing and the zero-energy edge states in the extended version of the CST-SSH model. For the Hamiltonian 5, we observe that various winding numbers—specifically  $-1, 0, 1,$  and  $2$ —can be realized by appropriately tuning the parameters  $(t_1, t_2, t_3, t_4)$ . Here, the winding number corresponds to the number of zero-energy edge modes per boundary under open boundary conditions.

For example, in Fig. 12, we choose  $(t_1, t_2, t_3, t_4) = (2, 1, -1, -4)$ , which yields a winding number of two. This is evident from the presence of two zero-energy edge states per boundary, observed for both  $\sigma = 0$  and  $\sigma = 1$ . The model can be further extended or modified to realize higher winding numbers.

Similar to the CST-SSH model discussed in the main text, the energy gap in the extended model gradually closes as a function of  $\sigma$ , and the zero-energy edge states become less localized. However, the application of  $\sigma$  does not alter the winding number, which was demonstrated in the Fig.10.

- 
- [1] A. Einstein, Die grundlage der allgemeinen relativitätstheorie [adp 49, 769 (1916)], *Annalen der Physik* **517**, 517 (2005).
  - [2] W. G. Unruh, Experimental black-hole evaporation?, *Physical Review Letters* **46**, 1351 (1981).
  - [3] R. Schützhold and W. G. Unruh, Gravity wave analogues of black holes, *Phys. Rev. D* **66**, 044019 (2002).
  - [4] G. E. Volovik, Superfluid analogies of cosmological phenomena, *Physics Reports* **351**, 195 (2001).
  - [5] M. Novello, V. De Lorenci, J. Salim, and R. Klippert, Geometrical aspects of light propagation in nonlinear electrodynamics, *Physical Review D* **61**, 045001 (2000).
  - [6] M. Novello and J. Salim, Effective electromagnetic geometry, *Physical Review D* **63**, 083511 (2001).
  - [7] B. Reznik, Origin of the thermal radiation in a solid-state analogue of a black hole, *Physical Review D* **62**, 044044 (2000).
  - [8] R. Schützhold, G. Plunien, and G. Soff, Dielectric black hole analogs, *Physical review letters* **88**, 061101 (2002).
  - [9] O. Lahav, A. Itah, A. Blumkin, C. Gordon, S. Rinott, A. Zayats, and J. Steinhauer, Realization of a sonic black hole analog in a bose-einstein condensate, *Phys. Rev. Lett.* **105**, 240401 (2010).
  - [10] L. J. Garay, J. R. Anglin, J. I. Cirac, and P. Zoller, Sonic analog of gravitational black holes in bose-einstein condensates, *Phys. Rev. Lett.* **85**, 4643 (2000).
  - [11] A. J. Kollár, M. Fitzpatrick, and A. A. Houck, Hyperbolic lattices in circuit quantum electrodynamics, *Nature* **571**, 45 (2019).

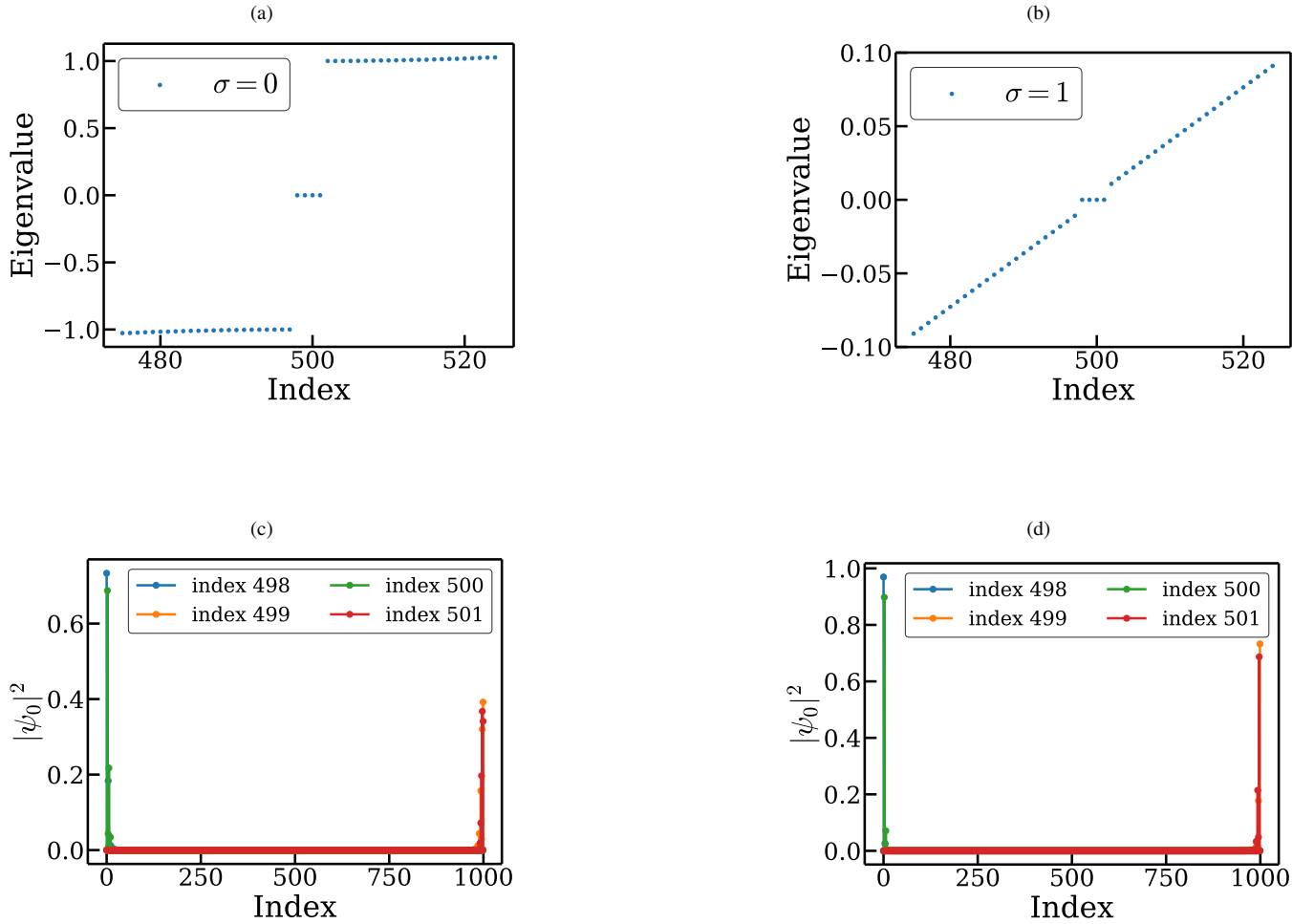


FIG. 12: Closing of the energy band gap and variation of zero energy eigen states variation with  $\sigma$ : for the extended CST-SSH model having system size  $2N = 1000$  (500 unit cells) with  $(t_1, t_2, t_3, t_4) = (2, 1, -1, -4)$ , which have a winding number 2. Top row (a),(b): Eigenvalue spectra for  $\sigma=0$  and 1, respectively. Bottom row (c),(d): Corresponding zero-energy eigenstates profiles.

- [12] H. S. Nguyen, D. Gerace, I. Carusotto, D. Sanvitto, E. Galopin, A. Lemaître, I. Sagnes, J. Bloch, and A. Amo, Acoustic black hole in a stationary hydrodynamic flow of microcavity polaritons, *Phys. Rev. Lett.* **114**, 036402 (2015).
- [13] B. Lapierre, K. Choo, C. Tauber, A. Tiwari, T. Neupert, and R. Chitra, Emergent black hole dynamics in critical floquet systems, *Phys. Rev. Res.* **2**, 023085 (2020).
- [14] B. Lapierre, T. Numasawa, T. Neupert, and S. Ryu, Floquet engineered inhomogeneous quantum chaos in critical systems (2024), arXiv:2405.01642 [cond-mat.str-el].
- [15] U. R. Fischer and R. Schützhold, Quantum simulation of cosmic inflation in two-component bose-einstein condensates, *Phys. Rev. A* **70**, 063615 (2004).
- [16] P. O. Fedichev and U. R. Fischer, Gibbons-hawking effect in the sonic de sitter space-time of an expanding bose-einstein-condensed gas, *Phys. Rev. Lett.* **91**, 240407 (2003).
- [17] Z. Tian, Y. Lin, U. R. Fischer, and J. Du, Testing the upper bound on the speed of scrambling with an analogue of hawking radiation using trapped ions, *The European Physical Journal C* **82**, 10.1140/epjc/s10052-022-10149-8 (2022).
- [18] C. C. H. Ribeiro, S.-S. Baak, and U. R. Fischer, Existence of steady-state black hole analogs in finite quasi-one-dimensional bose-einstein condensates, *Phys. Rev. D* **105**, 124066 (2022).
- [19] S. Sachdev and J. Ye, Gapless spin-fluid ground state in a random quantum heisenberg magnet, *Phys. Rev. Lett.* **70**, 3339 (1993).
- [20] J. Maldacena and D. Stanford, Remarks on the sachdev-ye-kitaev model, *Phys. Rev. D* **94**, 106002 (2016).
- [21] A. Kitaev and S. J. Suh, The soft mode in the sachdev-ye-kitaev model and its gravity dual, *Journal of High Energy Physics* **2018**, 1 (2018).
- [22] S.-Z. Li, X.-J. Yu, S.-L. Zhu, and Z. Li, Anderson localization and swing mobility edge in curved spacetime, *Physical Review B* **108**, 094209 (2023).
- [23] L. Mertens, A. G. Moghaddam, D. Chernyavsky, C. Morice, J. van Den Brink, and J. van Wezel, Thermalization by a syn-

- thetic horizon, *Physical Review Research* **4**, 043084 (2022).
- [24] C. Morice, D. Chernyavsky, J. van Wezel, J. van den Brink, and A. Moghaddam, Quantum dynamics in 1d lattice models with synthetic horizons, *SciPost Physics Core* **5**, 042 (2022).
- [25] C. Morice, A. G. Moghaddam, D. Chernyavsky, J. van Wezel, and J. van den Brink, Synthetic gravitational horizons in low-dimensional quantum matter, *Physical Review Research* **3**, L022022 (2021).
- [26] D. J. Thouless, M. Kohmoto, M. P. Nightingale, and M. den Nijs, Quantized hall conductance in a two-dimensional periodic potential, *Phys. Rev. Lett.* **49**, 405 (1982).
- [27] C. L. Kane and E. J. Mele, Quantum spin hall effect in graphene, *Phys. Rev. Lett.* **95**, 226801 (2005).
- [28] L. Fu, C. L. Kane, and E. J. Mele, Topological insulators in three dimensions, *Phys. Rev. Lett.* **98**, 106803 (2007).
- [29] B. A. Bernevig, T. L. Hughes, and S.-C. Zhang, Quantum spin hall effect and topological phase transition in hgte quantum wells, *science* **314**, 1757 (2006).
- [30] D. Hsieh, D. Qian, L. Wray, Y. Xia, Y. S. Hor, R. J. Cava, and M. Z. Hasan, A topological dirac insulator in a quantum spin hall phase, *Nature* **452**, 970 (2008).
- [31] Y. Chen, J. G. Analytis, J.-H. Chu, Z. Liu, S.-K. Mo, X.-L. Qi, H. Zhang, D. Lu, X. Dai, Z. Fang, et al., Experimental realization of a three-dimensional topological insulator, *bi2te3*, *science* **325**, 178 (2009).
- [32] C.-Z. Chang, J. Zhang, X. Feng, J. Shen, Z. Zhang, M. Guo, K. Li, Y. Ou, P. Wei, L.-L. Wang, et al., Experimental observation of the quantum anomalous hall effect in a magnetic topological insulator, *Science* **340**, 167 (2013).
- [33] L. Fu, Topological crystalline insulators, *Phys. Rev. Lett.* **106**, 106802 (2011).
- [34] Y. Tanaka, Z. Ren, T. Sato, K. Nakayama, S. Souma, T. Takahashi, K. Segawa, and Y. Ando, Experimental realization of a topological crystalline insulator in snte, *Nature Physics* **8**, 800 (2012).
- [35] P. Dziawa, B. Kowalski, K. Dybko, R. Buczko, A. Szczerbakow, M. Szot, E. Lusakowska, T. Balasubramanian, B. M. Wojek, M. Berntsen, et al., Topological crystalline insulator states in pb1-x sn x se, *Nature materials* **11**, 1023 (2012).
- [36] A. A. Burkov and L. Balents, Weyl semimetal in a topological insulator multilayer, *Phys. Rev. Lett.* **107**, 127205 (2011).
- [37] A. A. Burkov and L. Balents, Weyl semimetal in a topological insulator multilayer, *Phys. Rev. Lett.* **107**, 127205 (2011).
- [38] S. Borisenko, Q. Gibson, D. Evtushinsky, V. Zabolotnyy, B. Büchner, and R. J. Cava, Experimental realization of a three-dimensional dirac semimetal, *Phys. Rev. Lett.* **113**, 027603 (2014).
- [39] H. Watanabe, H. C. Po, M. P. Zaletel, and A. Vishwanath, Filling-enforced gaplessness in band structures of the 230 space groups, *Phys. Rev. Lett.* **117**, 096404 (2016).
- [40] W.-P. Su, J. Schrieffer, and A. Heeger, Soliton excitations in polyacetylene, *Physical Review B* **22**, 2099 (1980).
- [41] H. Takayama, Y. R. Lin-Liu, and K. Maki, Continuum model for solitons in polyacetylene, *Phys. Rev. B* **21**, 2388 (1980).
- [42] S. Kivelson and D. E. Heim, Hubbard versus peierls and the su-schrieffer-heeger model of polyacetylene, *Phys. Rev. B* **26**, 4278 (1982).
- [43] A. J. Heeger, S. Kivelson, J. R. Schrieffer, and W. P. Su, Solitons in conducting polymers, *Rev. Mod. Phys.* **60**, 781 (1988).
- [44] D. Joshi and T. Nag, Adiabatic charge transport in extended ssh models, *arXiv preprint arXiv:2503.18125* (2025).
- [45] E. J. Meier, F. A. An, and B. Gadway, Observation of the topological soliton state in the su-schrieffer-heeger model, *Nature communications* **7**, 13986 (2016).
- [46] C. Morice, D. Chernyavsky, J. van Wezel, J. van den Brink, and A. Moghaddam, Quantum dynamics in 1d lattice models with synthetic horizons, *SciPost Physics Core* **5**, 10.21468/scipost-physicscore.5.3.042 (2022).
- [47] C. Y. Wong, T. H. Hui, P. D. Sacramento, and W. C. Yu, Entanglement in quenched extended su-schrieffer-heeger model with anomalous dynamical quantum phase transitions, *Phys. Rev. B* **110**, 054312 (2024).
- [48] G. Jin, D. O. Oriekhov, L. J. Splitthoff, and E. Greplova, Topological finite size effect in one-dimensional chiral symmetric systems (2024), *arXiv:2411.17822 [cond-mat.mes-hall]*.
- [49] T. Mishra, J. Carrasquilla, and M. Rigol, Phase diagram of the half-filled one-dimensional  $t-v-V'$  model, *Phys. Rev. B* **84**, 115135 (2011).
- [50] J. K. Asbóth, L. Oroszlány, and A. Pályi, *A Short Course on Topological Insulators* (Springer International Publishing, 2016).
- [51] A. Altland and M. R. Zirnbauer, Nonstandard symmetry classes in mesoscopic normal-superconducting hybrid structures, *Physical Review B* **55**, 1142–1161 (1997).
- [52] S. Ryu, A. P. Schnyder, A. Furusaki, and A. W. W. Ludwig, Topological insulators and superconductors: tenfold way and dimensional hierarchy, *New Journal of Physics* **12**, 065010 (2010).
- [53] X. Shi, I. Kiorpelidis, R. Chaunsali, V. Achilleos, G. Theoharis, and J. Yang, Disorder-induced topological phase transition in a one-dimensional mechanical system, *Phys. Rev. Res.* **3**, 033012 (2021).
- [54] E. J. Meier, F. A. An, A. Dauphin, M. Maffei, P. Massignan, T. L. Hughes, and B. Gadway, Observation of the topological anderson insulator in disordered atomic wires, *Science* **362**, 929 (2018).
- [55] F. Cardano, A. D'Errico, A. Dauphin, M. Maffei, B. Piccirilli, C. de Lisi, G. De Filippis, V. Cataudella, E. Santamato, L. Marrucci, M. Lewenstein, and P. Massignan, Detection of zak phases and topological invariants in a chiral quantum walk of twisted photons, *Nature Communications* **8**, 10.1038/ncomms15516 (2017).
- [56] A. Ghosh, A. M. Martin, and S. Majumder, Quench dynamics of edge states in a finite extended su-schrieffer-heeger system, *Phys. Rev. E* **108**, 034102 (2023).
- [57] M. Suman, S. Aravinda, and R. Modak, Probing quantum phase transitions via quantum speed limits, *Phys. Rev. A* **110**, 012466 (2024).
- [58] D.-W. Zhang, Y.-Q. Zhu, Y. Zhao, H. Yan, and S.-L. Zhu, Topological quantum matter with cold atoms, *Advances in Physics* **67**, 253 (2018).
- [59] C. Viermann, M. Sparn, N. Liebster, M. Hans, E. Kath, Á. Parra-López, M. Tolosa-Simeón, N. Sánchez-Kuntz, T. Haas, H. Strobel, et al., Quantum field simulator for dynamics in curved spacetime, *nature* **611**, 260 (2022).
- [60] C. Barceló, Analogue black-hole horizons, *Nature Physics* **15**, 210 (2019).
- [61] L. Viotti, A. L. Gramajo, P. I. Villar, F. C. Lombardo, and R. Fazio, Geometric phases along quantum trajectories, *Quantum* **7**, 1029 (2023).
- [62] V. Könye, C. Morice, D. Chernyavsky, A. G. Moghaddam, J. van den Brink, and J. van Wezel, Horizon physics of quasi-one-dimensional tilted weyl cones on a lattice, *Phys. Rev. Res.* **4**, 033237 (2022).
- [63] L. Mertens, A. G. Moghaddam, D. Chernyavsky, C. Morice, J. van den Brink, and J. van Wezel, Thermalization by a synthetic horizon, *Phys. Rev. Res.* **4**, 043084 (2022).

- [64] R. He, Y. Zhao, C. Sheng, J. Duan, Y. Wei, C. Sun, L. Lu, Y.-X. Gong, S. Zhu, and H. Liu, Experimental realization of quantum walks near synthetic horizons on photonic lattices, *Phys. Rev. Res.* **6**, 013233 (2024).
- [65] C. D. Beule, S. Groenendijk, T. Meng, and T. L. Schmidt, Artificial event horizons in Weyl semimetal heterostructures and their non-equilibrium signatures, *SciPost Phys.* **11**, 095 (2021).
- [66] A. G. Moghaddam, D. Chernyavsky, C. Morice, J. van Wezel, and J. van den Brink, Engineering spectral properties of non-interacting lattice Hamiltonians, *SciPost Phys.* **11**, 109 (2021).